PNAS RESEARCH ARTICLE | MEDICAL SCIENCES

Obesity triggers tumoral senescence and renders poorly immunogenic malignancies amenable to senolysis

Frédérik Fournier[a], Roberto Diaz-Marin[a], Frédérique Pilon[b], Mathieu Neault[a], Rachel Juneau[b], Gabrielle Girouard[c], Ariel M. Wilson[b], Bruno Larrivée[b], Frédérick A. Mallette[a,d], Sergio Crespo-Garcia[a,1,2], and Przemyslaw Sapieha[a,b,e,2]

Edited by Napoleone Ferrara, University of California San Diego, La Jolla, CA; received June 10, 2022; accepted November 17, 2022

Obesity is a major risk factor for cancer. Conventional thought suggests that elevated adiposity predisposes to heightened inflammatory stress and potentiates tumor growth, yet underlying mechanisms remain ill-defined. Here, we show that tumors from patients with a body mass index >35 carry a high burden of senescent cells. In mouse syngeneic tumor models, we correlated a pronounced accretion of senescent cancer cells with poorly immunogenic tumors when mice were subjected to diet-induced obesity (DIO). Highly immunogenic tumors showed lesser senescence burden suggesting immune-mediated elimination of senescent cancer cells, likely targeted as a consequence of their senescence-associated secretory phenotype. Treatment with the senolytic BH3 mimetic small molecule inhibitor ABT-263 selectively stalled tumor growth in mice with DIO to rates comparable to regular diet-fed mice. Thus, consideration of body adiposity in the selection of cancer therapy may be a critical determinant for disease outcome in poorly immunogenic malignancies.

cancer | obesity | senescence | immunogenicity

Obesity constitutes a major modifiable risk factor for cancer. Worldwide, around 12% of cancers in men and 13% of cancers in women are estimated to be attributable to obesity (1). In the United States, it is believed that 20% of all cancer-related deaths in women and 14% in men over the age of 50 correlate with being overweight or obese (2). These numbers will continue to rise as developed and developing countries see steep increases in populational rates of obesity (3). Despite extensive research efforts, the cellular and molecular mechanisms by which tumor growth is triggered and driven by obesity remain poorly understood but several lines of evidence point to elevated systemic inflammation and cytokine levels (1, 4–8).

A potential contribution to the rise in inflammatory factors in obesity may come from subsets of cells that have entered a senescent state (9–12). Cellular senescence is associated with growth arrest in mitotic cells and often interchangeably associated with aging; yet, it can be triggered in younger organisms secondary to cellular, DNA, and organelle damage (reviewed in ref. 13). It is involved in physiological development (14, 15) and wound healing (16) but can conversely exacerbate several aging-associated diseases such as retinopathies (17–19) and cancer (20, 21). Aging and obesity accelerate the accumulation of senescent cells in several organs and tissues contributing to deleterious changes in body weight and composition, cardiac and metabolic health, insulin resistance as well as hepatic steatosis (22–24).

High adiposity is reported to accelerate phenotypes associated with aging, promote cellular senescence, and provoke a state of cytokine production called the senescence-associated secretory phenotype (SASP) (25–30). Cellular growth arrest that leads to senescence is thought to have evolved as a protective mechanism to limit tumor growth. However, if sustained, senescent cells within the tumor may accelerate cancer cell proliferation through SASP-induced inflammation and potentially epithelial to mesenchymal transition (EMT) (21, 31, 32). Among the many proteins that are part of the SASP, senescent cells can secrete metalloproteinases (e.g., MMP-2 and MMP-3) (33, 34), proteases (such as uPA and its regulator, PAI-1) (35, 36), and interleukins such as IL6 and IL8 (37), which participate in cell migration. Malignant masses harboring senescent cells have also been reported to express various chemokines (e.g., CSF-1, CXCL-1, and MCP-1) responsible for immune infiltration (38).

Senescent cells become reliant on prosurvival pathways such as those regulated by the B cell lymphoma protein-2 (BCL-2) family (39–43). Members of this family such as BCL-2, BCL-xL, BCL-w, and MCL1 inhibit the proapoptotic action of BAX or BAK through direct binding (44). Hence, while originally developed for use in oncology, BCL-2 family inhibitors or BH3-(BCL-2 homology region 3) mimetics can be used to steer senescent cells down an apoptotic path. For example, drugs such as navitoclax (ABT-263) which binds BCL-2, BCL-xL, and BCL-w have shown promising preclinical results

Significance

Obesity is a major cancer risk factor and the mechanisms driving tumor growth remain poorly understood. We found that tumors from patients with a body mass index >35 carry a high burden of senescent cells. While classically associated with aging, cellular senescence can also be triggered by cellular damage. Senescent cells produce a broad secretome of inflammatory factors that, when persistent, may itself exacerbate tissue damage and accelerate tumor growth. We found that poorly immunogenic tumors in obese mice grow rapidly and have high numbers of senescent cells. A drug that kills senescent cells (senolytic) stalled tumor growth to rates comparable to lean mice. Our findings suggest that a patient's body adiposity should be considered when selecting cancer therapies.

Author contributions: F.F., S.C.-G., and P.S. designed research; F.F., R.D.-M., F.P., M.N., R.J., G.G., A.M.W., and S.C.-G. performed research; B.L., F.A.M., and P.S. contributed new reagents/analytic tools; F.F. and R.D.-M. analyzed data; and F.F., A.M.W., S.C.-G., and P.S. wrote the paper.

Competing interest statement: P.S. is the Chief Scientific Advisor at UNITY Biotechnology. The rest of the authors have no competing interests.

This article is a PNAS Direct Submission.

[1]Present address: École d'optométrie, Université de Montréal, Montréal, QC H3T 1P1, Canada.

[2]To whom correspondence may be addressed: Email: mike.sapieha@umontreal.ca or sergio.crespo.garcia@umontreal.ca.

This article contains supporting information online at https://www.pnas.org/lookup/suppl/doi:10.1073/pnas.2209973120/-/DCSupplemental.

Published December 27, 2022.

through their senolytic activity in mitigating several age-related pathologies and conditions associated with cellular damage (18, 45–47). However, there has been limited success for ABT-263 in oncology, due to potential side effects (48–50) and limited single-agent efficacy (51). Consequently, it is mainly used in combination therapy in oncology (12, 52–57) potentially because a cancer's cell reliance on BCL-2 family members may vary depending on the stressors that instigated senescence (58).

In the current study, we observed that obese patients with colorectal cancer (CRC) metastasis in the liver and who were unresponsive to treatment had a significant number of senescent cells associated with malignant regions. We developed a senescence-associated (SA)-β-galactosidase (gal) single-cell detection assay that allowed us to correlate the elevated burden of senescent cancer cells to poorly immunogenic tumors in syngeneic tumor mouse models. We demonstrate that diet-induced obesity (DIO) is a trigger for cellular senescence in rapidly forming and poorly immunogenic tumors. Using ABT-263 as a proof of concept of senolysis, we targeted senescent cancer cells and stalled tumor growth to rates seen in lean mice. Our data provide a rationale for pharmacological intervention using targeted senolysis for tumors in individuals with elevated body mass indexs (BMIs).

Results

DIO Potentiates Tumor Growth and Triggers Tumoral Senescence in Poorly Immunogenic Tumors. Obesity can impair immune function, impacting the strength of tumoral immunity and potentially yielding a tumoral microenvironment (TME) permissive for cancer cell proliferation (30, 59). Obesity can also alter TME metabolism to suppress antitumor immunity (60). Reduced immunogenicity and an immunosuppressive TME are both characteristics of poorly immunogenic tumors. Senescent cells, usually cleared by natural killer cells, macrophages, neutrophils, and T cells, may survive and accumulate in poorly immunogenic tumors because of suboptimal immune surveillance (17, 61).

In order to investigate the link between adiposity and senescence in poorly immunogenic tumors, we assessed the burden of senescent cells in human histological samples from obese patients (BMI > 35) with CRC. In hepatic metastasis biopsies from these patients, we found elevated expression of the cell cycle arrest marker $p16^{INK4A}$ and the SASP protein PAI-1 when compared to samples from lean patients (BMI < 25) (Fig. 1*A*). Notably, $p16^{INK4A}$-positive cells were ∼fourfold more abundant in tumoral regions than in healthy hepatic regions of obese patients (Fig. 1*B* and *SI Appendix*, Fig. S1 *A* and *B*). Dashed lines delimit between healthy (H) and tumoral (T) tissues. Biopsies from lean patients did not show any difference in the expression of $p16^{INK4A}$ between tumoral and healthy regions, suggesting that $p16^{INK4A}$ expression in tumors was driven by elevated BMI.

To explore the consequences of cellular senescence on tumor growth during obesity, we modeled the paradigm with xenografts in mice undergoing DIO. We randomized male *C57Bl/6J* mice to either *ad libitum* high-fat diets (60% fat calories) or nutritionally matched control chow diets (10% fat calories). After 1 mo of diet, the feeding paradigms lead to mice with significant differences in weight (*SI Appendix*, Fig. S1*C*) and glucose metabolism as evaluated by the glucose tolerance test (GTT) (*SI Appendix*, Fig. S1*D*) and insulin tolerance test (ITT) (*SI Appendix*, Fig. S1*E*). Subsequently, obese mice were inoculated with syngeneic tumor models from cancer cell lines presenting different levels of immunogenicity: poorly immunogenic Lewis lung carcinoma cells (LLC), moderately immunogenic melanoma cells (B16-F10), or highly immunogenic colon adenocarcinoma cells (MC-38) (Fig. 1 *C–E* and *SI Appendix*, Fig. S1*F*) (62–64). Consistent with the notion that obesity potentiates cancer development, for all cancer cell lines, we observed significantly augmented tumor growth during DIO starting on the 1st wk after inoculation (Fig. 1 *C–E*).

Next, we characterized the presence of senescent cells in each of the three syngeneic tumor lines. Senescence-associated β-galactosidase (SA-β-gal) activity was robustly increased in LLC tumors of DIO mice (Fig. 1*F*) and to a lesser extent in B16-F10 syngeneic tumors in high-fat diet-fed mice (Fig. 1*G*). Conversely, MC-38 tumors, which are the most immunogenic, did not show SA-β-gal activity (Fig. 1*H*). In addition, Western blot analysis revealed that syngeneic tumors from LLC also showed a high-fat diet-dependent increase in senescence markers PAI-1, BCL-xL, BCL-2, and $p16^{INK4a}$ (Fig. 1 *I–O*). The levels of $p21^{CIP1}$ were not significantly elevated yet slightly trended to increase. In contrast, these markers did not vary in tumors from either B16-F10 or MC-38 cell lines (Fig. 1 *I–O*). Moreover, the transcription of several SASP-related factors such as *Il6, Vegfa, Tgfb*, and *Nos2* was significantly increased in LLC tumors from DIO mice (Fig. 1*P*). From all the SASP-related factors that were assessed, transcripts for *Il6* and *Vegfa* were also significantly increased in B16-F10 tumors from DIO mice (*SI Appendix*, Fig. S1*G*). Collectively, our data suggest an inverse correlation between tumoral senescence and tumoral immunogenicity.

Therapeutic Senolysis with ABT-263 Hinders Obesity-Driven Tumor Growth in Poorly Immunogenic Tumors. Given the elevated levels of BCL-2 family proteins in LLC tumors after DIO (Fig. 1), we next sought to determine the therapeutic merit of senolysis for poorly immunogenic LLC tumors during obesity. We opted to target senescent cells with the small-molecule BCL-2/BCL-xL/BCL-w inhibitor ABT-263 (39, 42). While ABT-263 is toxic toward platelets and neutrophils (48, 65) and has limited single-agent use in clinic, we used the compound to establish a proof-of-concept for senolysis in obesity-driven tumor growth. We treated mice with DIO by gavage for five consecutive days with either ABT-263 (75 mg/kg) or DMSO vehicle, starting 7 d post tumor inoculation and assessed tumor growth by caliper volumetric measurements (Fig. 2*A*).

ABT-263 significantly reduced the size of poorly immunogenic LLC tumors as well as moderately immunogenic B16-F10 tumors in mice subjected to DIO but had no effect on growth of immunogenic MC-38 tumors (Fig. 2 *B–D*). We next evaluated the specificity of senolysis by measuring SA-β-gal activity with an adapted protocol (66) using the 5-dodecanoylaminofluorescein di-β-D-galactopyranoside (C_{12}FDG) substrate for β-galactosidase in vivo (*SI Appendix*, Fig. S2*A*). In mice inoculated with LLC cells, treatment with ABT-263 reduced the percentage of $C_{12}FDG^{+}$ cells by ∼twofold (Fig. 2 *E* and *F*). Conversely, mice inoculated with more immunogenic B16-F10 or highly immunogenic MC-38 tumors

and (*O*) $p16^{INK4a}$ in tumor lysates. Data are normalized to their respective cancer cell line CTRL and shown as folds. (*P*) Bar charts represent analysis of SASP-related factors using mRNA expression of *Il6, Vegfa, Tgfb1, Nos2, and Serpine1* in whole LLC-tumor lysates. Human data represent three independent samples. WB data represent n ≥ 3 from independent experiments. Statistics: (*B*) One-way ANOVA and Bonferroni *post hoc* test (*C–E*) Two-way ANOVA and Bonferroni *post hoc* test. (*J–P*) Two-tailed unpaired Student's *t* test. * $P < 0.05$, ** $P < 0.01$, *** $P < 0.001$; 95% CI. Error bars represent mean ± SEM. Each *n* represents biological replicates.

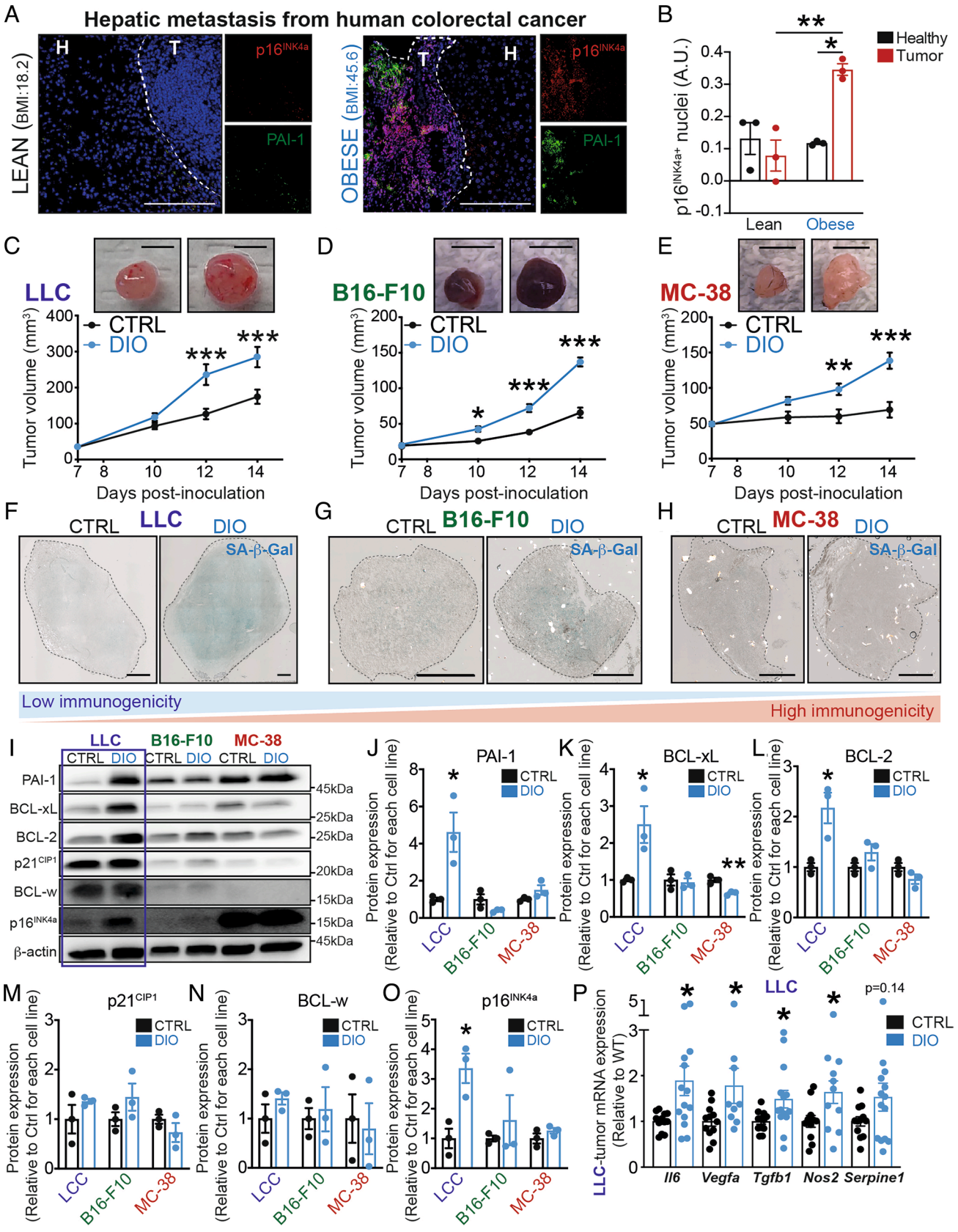

Fig. 1. Diet-induced obesity potentiates tumor growth and triggers tumoral senescence in poorly immunogenic tumors. (*A*) Representative immunofluorescence images showing p16^{INK4a} (in red), PAI-1 (in green), and merged images with DAPI (in blue) in lean and obese patients. Dashed lines delimit between healthy (H) and tumoral (T) tissues (scale bar, 200 μm). (*B*) Bar charts represent colocalization analysis between p16^{INK4a} and DAPI within healthy and tumoral regions using Pearson's correlation. (*C*–*E*) Volumetric analysis of tumor growth, using caliper, of mice under DIO and CTRL-fed mice in a time course after (*C*) LLC, (*D*) B16-F10, or (*E*) MC-38 inoculation at 7, 10, 12, and 14 d (scale bar, 5 mm). (*F*–*H*) Representative images of senescence-associated β-galactosidase activity (SA-β-Gal) on (*F*) LLC, (*G*) B16-F10, or (*H*) MC-38 tumor cross sections (scale bar, 1,000 μm). (*I*) Representative WB images of markers of cellular senescence in whole LLC, B16-F10, and MC-38 tumors of mice under DIO or CTRL-fed diet. (*J*–*O*) Bar charts represent quantification of protein levels of (*J*) PAI-1, (*K*) BCL-xL, (*L*) BCL-2, (*M*) p21^{CIP1}, (*N*) BCL-w,

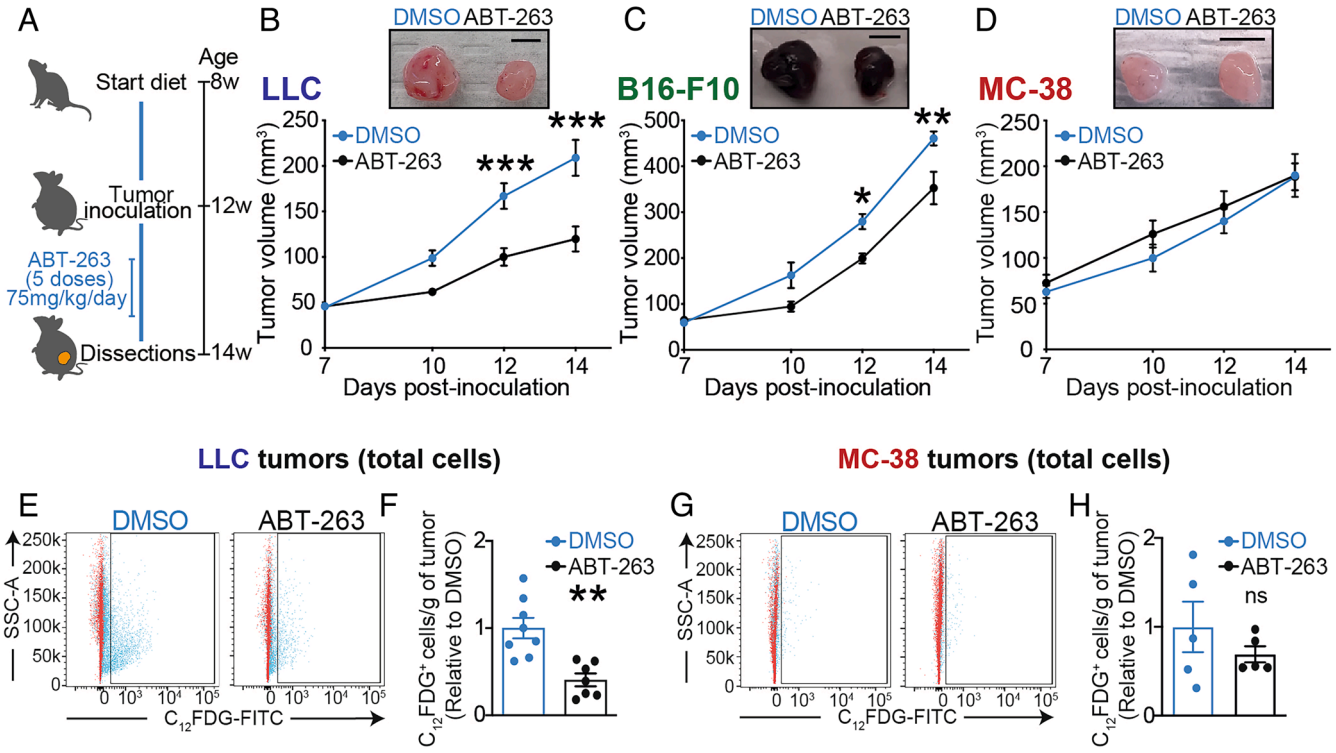

Fig. 2. Therapeutic senolysis hinders obesity-driven tumor growth in poorly immunogenic tumors. (*A*) Schematic representation of the experimental paradigm combining diet-induced obesity with ABT-263 treatment. (*B–D*) Curve represents tumor growth in vivo using caliper volumetric measurements of (*B*) LLC, (*C*) B16-F10, or (*D*) MC-38 cells. (*E–H*) Representative FACS histograms and quantification of $C_{12}FDG^+$ cells in (*E*, *F*) LLC tumors or (*G*, *H*) MC-38 tumors from DMSO- or ABT-treated mice. Bar charts indicate the relative number of $C_{12}FDG^+$ cells per gram of tumor. Tumor monitoring and FACS data represent ≥2 independent experiments with n ≥ 5 biological replicates. Statistics: (*B–D*) Two-way ANOVA and Bonferroni post hoc test. (*F*, *H*) Two-tailed unpaired Student's *t* test. * or § $P < 0.05$, ** or §§ $P < 0.01$, *** or §§§ $P < 0.001$; 95% CI. Error bars represent mean ± SEM. Each *n* represents biological replicates

were largely irresponsive to treatment with ABT-263 (Fig. 2 *G* and *H* and *SI Appendix*, Fig. S2 *B–F*). The inverse correlation between tumoral immunogenicity and tumoral senescence was further substantiated as treatment with ABT-263 reduced weight of LLC tumors (by 1.6-fold; *SI Appendix*, Fig. S2*G*). Notably, following ABT-263, we observed a modest nonsignificant reduction in tumor weight in mice inoculated with B16-F10 cells (*SI Appendix*, Fig. S2*H*), without reduction in $C_{12}FDG^+$ cells (*SI Appendix*, Fig. S2*E*) suggesting a nonsenolytic mechanism contributing to reduction in the tumor volume. These data are consistent with low levels of senescence (low expression of SA-β-gal activity and BCL-2 family proteins) in B16-F10 tumors (Fig. 1 *G*, *K*, and *L*). The weight of MC-38 tumors did not vary with ABT-263 (*SI Appendix*, Fig. S2*I*). Together, these results underscore the different response rates to a BCL-2/BCL-xL/BCL-w inhibitor of poorly immunogenic tumors, with elevated senescent cell burden (22.2 to 13.3%) versus highly immunogenic tumors with low numbers of senescent cells (2.9 to 2.0%) (*SI Appendix*, Fig. S2*J*).

ABT-263 Triggers Tumoral Apoptosis and Impedes Tumor Growth in DIO to Rates Observed in Nonobese Mice. Given the ability of ABT-263 to impede the rate of growth of LLC tumors, we next assessed the mechanism by which cells are being eliminated. Mechanism engagement of ABT-263 was verified in vivo in LLC tumors. First, we evaluated how rapidly ABT-263 can induce apoptosis. Upon a single dose of ABT-263, we observed a twofold increase in cleaved-caspase 3 in tumor lysates (Fig. 3 *A* and *B*). Second, we performed a time course of caspase 3 and caspase 7 activation to evaluate the impact of ABT-263 treatment course (5 doses) and if cancer cell apoptosis persisted at the time of assessment of senescence (14 d postinoculation of the tumor and 7 d postadministration of treatment). Mice treated with ABT-263 had consistently higher levels of tumor-cell apoptosis at all time points examined (Fig. 3*C*).

To gain insight into the kinetics of reduction of tumor growth with ABT-263, we transduced the LLC cell line with mCherry and luciferase reporters ($LLC^{mCherryLuc}$) to allow in vivo tumor monitoring and complementary ex vivo analyses (*SI Appendix*, Fig. S3 *A* and *B*). The stability of the transgene, as well as its impact on proliferation and viability of LLC cells, was verified (*SI Appendix*, Fig. S3 *C* and *D*), confirming that tumor phenotypes and growth rates were maintained when on DIO (Figs. 1 and 2 and *SI Appendix*, Fig. S3 *E* and *F*). In vivo imaging of tumors in mice with DIO revealed that ABT-263 significantly decreased the growth rate of inoculated tumors from $LLC^{mCherryLuc}$ cells and brought them to rates observed in nonobese control (CTRL) mice (Fig. 3 *D* and *E*).

ABT-263 Selectively Eliminates Growth-Arrested Cancer Cells through the Induction of Apoptosis in Poorly Immunogenic Tumors with DIO. To assess the impact of ABT-263 on distinct cell populations within the tumor, we performed FACS analysis in naive and $C_{12}FDG$-labelled tumors to determine the identity of senescent cells that were being eliminated. We gated on tumor-associated macrophages (TAMs) ($Zombie^-$, $CD45.2^+$, $CD11b^+$, $Ly6G^-$, $CD11c^{-/low}$ (to discriminate DCs), $F4/80^{high}$, and $CD64^+$), tumor-associated neutrophils (TANs) ($Zombie^-$, $CD45.2^+$, $CD11b^+$, and $Ly\text{-}6G^{high}$), and tumor-associated endothelial cells (TAECs) ($Zombie^-$, $CD45.2^-$, and $CD31^+$). ABT-263 did not reduce the numbers of total or $C_{12}FDG^+$ TAMs (Fig. 4 *A–D* and *SI Appendix*, Fig. S4 *A* and *B*), total or $C_{12}FDG^+$ TANs (Fig. 4 *E–H* and *SI Appendix*, Fig. S4*C*), nor total or $C_{12}FDG^+$ TAECs (Fig. 4

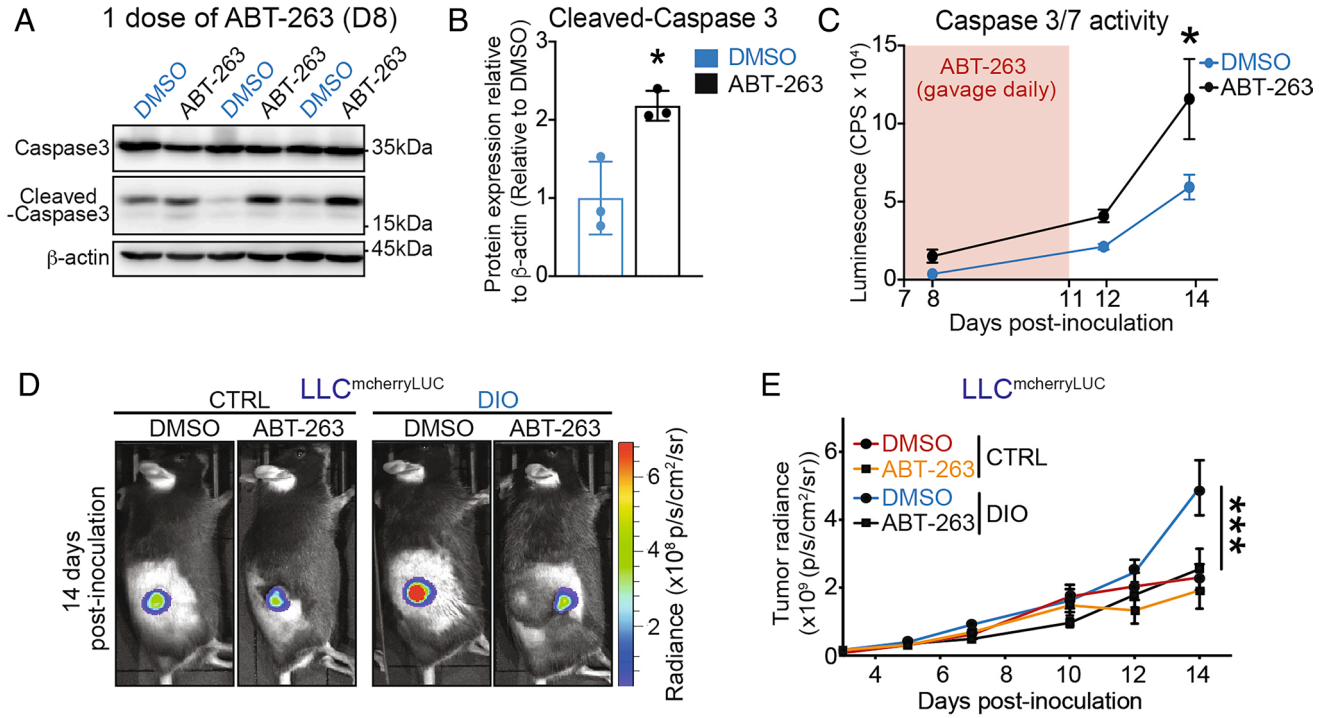

Fig. 3. ABT-263 triggers tumoral apoptosis and impedes tumor growth in DIO to rates observed in nonobese mice. (*A*) Representative WB images of caspase 3 and cleaved-caspase 3 in whole LLC tumors from mice in DIO after a single dose of ABT-263 or DMSO. (*B*) Bar charts represent the quantification of protein levels of caspase 3 and cleaved-caspase3 in tumor lysates. Data are normalized to DMSO and shown as folds. (*C*) Curve represents caspase 3 and caspase7 activation at 1 (D8 after inoculation), 5 (D12 after inoculation), and 7 (D14 after inoculation) days after the first dose of either ABT-263 or DMSO. Luminescence signal was reported as CPS. (*D*) Representative images of tumors in vivo from ABT-263-treated and control mice at 14 d postinoculation of LLC cells obtained with *IVIS*. Images overlay the luminescent signals and are represented as radiance (p/s/cm^2/sr). Imaging thresholds were optimized for minimizing interbatch variation (min: 4.00e7; max:6.90e8). (*E*) Curve represents tumor growth in vivo using luciferase activity by means of *IVIS*. Apoptosis data represent three biological replicates per time point. Tumor monitoring data represent ≥2 independent experiments with n ≥ 4 biological replicates. Statistics: (*B*) Two-tailed unpaired Student's *t* test. (*C*, *E*) Two-way ANOVA and Bonferroni *post hoc* test. *P < 0.05, **P < 0.01, ***P < 0.001; 95% CI. Outliers were determined with the ROUT method (Q = 1, 0%). Error bars represent mean ± SEM. Each *n* represents biological replicates.

I–*L* and *SI Appendix*, Fig. S4*D*). Importantly, ABT-263 selectively eliminated mCherry$^+$ cancer cells and mCherry$^+$ $C_{12}FDG^+$ cells by ~35% compared to DMSO controls (Fig. 4 *M*–*P* and *SI Appendix*, Fig. S4*E*). These data suggest that, in obesity, $C_{12}FDG^+$ cancer cells of poorly immunogenic tumors are selectively susceptible to therapeutic elimination through the inhibition of BCL-2 family members.

To confirm that $C_{12}FDG^+$ LLC cells were in a state of cellular senescence, we assessed the cell cycle status of viable cancer cells within implanted tumors (*SI Appendix*, Fig. S4*F*). Following treatment with ABT-263, the number of LLC cells in G0/G1 phases was significantly decreased (DMSO: 21.75%; ABT-263: 12.64%) and proportionately compensated by an increase in cells in G2/M phases (DMSO: 72.16%; ABT-263: 80.56%) (Fig. 4 *Q* and *R*). These data are consistent with the accretion of senescent cancer cells during DIO, where $C_{12}FDG^+$ LLC cells undergo cell cycle arrest in G0/G1 (Fig. 4*S*). ABT-263 did not reduce the tumor growth or presence of $C_{12}FDG^+$ cells in CTRL mice which further underscores its specificity for cancer cells in mice with DIO (*SI Appendix*, Fig. S4*A*). In sum, obesity-driven tumor growth in poorly immunogenic tumors is impeded by selectively triggering apoptosis of senescent cancer cells through the inhibition of BCL-2 protein family members with ABT-263 (Fig. 5*A*).

Discussion

Epidemiological studies have established an association between adiposity and cancer (2, 67), yet biological links remain elusive. In this study, we explored the possibility that high adiposity could trigger tumoral cell senescence and foment tumor growth. We provide evidence that p16^{INK4a}–positive cells trend with proliferative lesions in obese patients with hepatic metastasis of CRC, that mice on DIO see exacerbated growth of tumors that is associated with heightened senescence burden in poorly immunogenic tumors and that senolysis with a BH-3 mimetic can revert tumor growth in obese mice to rates observed in lean mice. Collectively, these data suggest that a patient's body adiposity should be considered in the selection of cancer therapy and may be an important determinant for the disease outcome.

Senescent cells accumulate in several organs during obesity, leading to fat accumulation, metabolic consequences, or even anxiety and neurogenesis (23, 24, 27, 68, 69). We found that obese patients with hepatic metastasis of CRC displayed high levels of p16^{INK4a}–positive cells within tumors that were associated with proliferative lesions. Although p16^{INK4a} can trigger protective cellular senescence, it can also be an indicator of unfavorable prognostic for a number of advanced stage malignancies (68, 69), in part due to the SASP that can fuel cancer development and growth (reviewed in refs. 13 and 56). During the metastatic phase of gastric cancer, which is characterized by poor treatment response, cancer cells acquire epithelial-to-mesenchymal-transition (EMT) properties through processes that have been associated with cellular senescence (70). Interestingly, we observed an inverse correlation between accretion of senescent cells and tumor immunogenicity profiles across various tumor cell lines. Within the timeframe of our experimental paradigm, low immunogenic LLC had higher burdens of senescence cells, while highly immunogenic MC-38 tumors were devoid of senescent cells. Moderately, immunogenic B16-F10 tumors showed

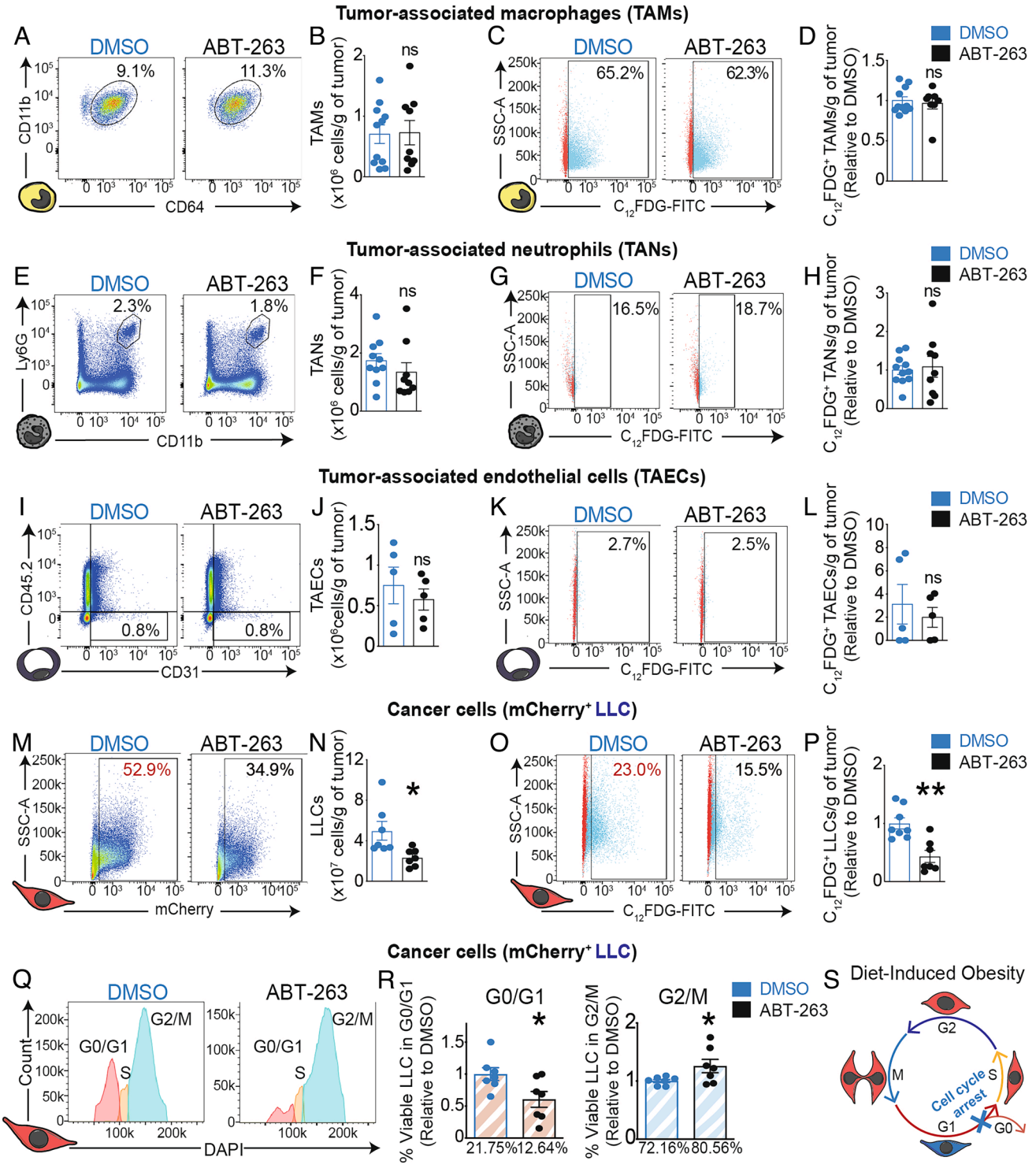

Fig. 4. ABT-263 selectively eliminates growth-arrested cancer cells through the induction of apoptosis in poorly immunogenic tumors with DIO. (*A–P*) Representative FACS histograms and quantification of (*A*, *B*) total and (*C*, *D*) $C_{12}FDG^+$ TAMs, (*E*, *F*) total and (*G*, *H*) $C_{12}FDG^+$ TANs, (*I*, *J*) total and (*K*, *L*) $C_{12}FDG^+$ TAECs, or (*M*, *N*) total and (*O*, *P*) $C_{12}FDG^+$ LLC cells in the TME. Percentages indicate proportion of tumor-associated TAMs, TANs, TAECs, or cancer cells to viable cells. Bar charts indicate the absolute number of cells from a given cell type per gram of tumor or the relative number of $C_{12}FDG^+$ cells from a given cell type per gram of tumor. (*Q*) Representative histograms depicting the cell cycle state of LLC cells within the TME. (*R*) Cell cycle analysis by FACS, represented as fold change to DMSO control in cancer cells at either the G0/G1 phase, or the G2/M phases. Percentages indicate proportions of LLC cells in the G0/G1 or the G2/M phase to total LLC cells. (*S*) Schematic representation of the cell cycle arrest of a $C_{12}FDG^+$ LLC cell in the G1 phase. FACS data represent ≥3 independent experiments with ≥5 biological replicates. Statistics: (*B*, *D*, *F*, *H*, *J*, *L*, *N*, *P*, *R*) Two-tailed unpaired Student's *t* test. $*P < 0.05$, $**P < 0.01$, $***P < 0.001$; 95% CI. Outliers were determined with the ROUT method (Q = 1, 0%). Error bars represent mean ± SEM. Each *n* represents biological replicates.

some evidence of cellular senescence. DIO has been shown to accelerate tumor growth in mice by influencing the TME and immune response, in part through impairing infiltration and function of $CD8^+$ T in highly immunogenic tumors such as MC38-derived (60). Our data provide additional evidence that tumoral senescence can further influence tumor development in poorly immunogenic tumors. Future investigations should determine if high fat diets themselves trigger cellular senescence in cancer cells, provide a TME

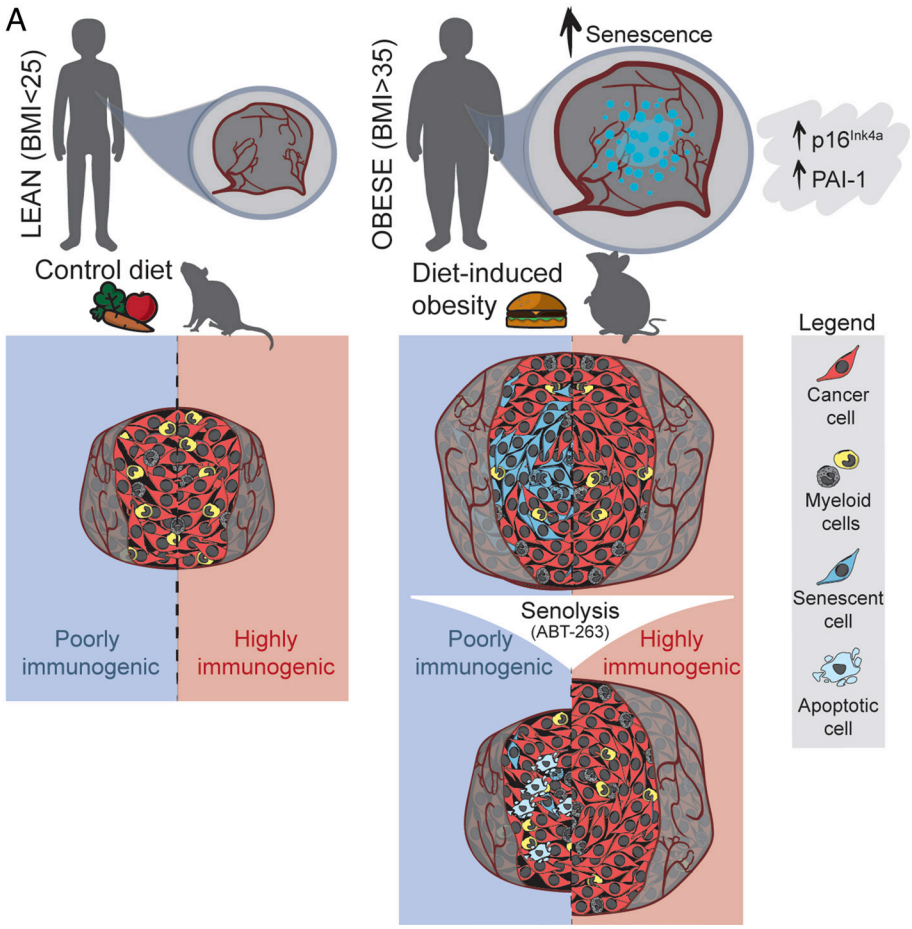

Fig. 5. Obesity triggers tumoral senescence and renders poorly immunogenic malignancies amenable to senolysis. Graphical abstract illustrating that obese patients and obese mice have increased burdens of senescent cancer cells when compared to lean individuals. In mice, elevated burdens of senescent cancer cells are associated with poorly immunogenic tumors. These tumors benefit from senolysis through inhibition of BCL-2 family members.

that is conducive for induction of cellular senescence, or accelerate cancer cell proliferation that ultimately triggers pathways of cellular senescence.

In obese mice, senolytic drugs can improve metabolic health (27, 71) and reduce hepatic steatosis (24). With the current study, we demonstrate that ABT-263, a broad inhibitor of prosurvival BCL-2 family members BCL-2/BCL-xL/BCL-w, can be used as a senolytic drug to limit the rapid tumor growth observed with DIO in poorly immunogenic tumors that are rich in senescent cells. ABT-263 is orally bioavailable and had entered phase I clinical trials for Non-Hodgkin Lymphoma and Chronic Lymphocytic Leukemia (72, 73). Responses were partial with little progression-free survival. Clinical development of ABT-263 was further limited by side effects such as thrombocytopenia and neutropenia with repeat use or high dose regimens (48, 65) due to inhibition of BCL-xL. While side effects can be managed through the implementation of a lead-in period, dose reduction, or the administration of G-CSF (filgrastim) in neutropenia (65, 73, 74), safer and more targeted BH3-mimetics such as ABT-199 (venetoclax) that spare BCL-xL have been developed (44). BCL-2 family inhibitors, such as ABT-263, can be potentiated through the inhibition of additional oncogenic pathways or direct activation of the BAX pathway (75–78). Moreover, combination therapy of ABT-263 with approved chemotherapeutic drugs such as Osimertinib or Trametinib has been explored in clinical trials for lung, ovarian, and skin cancers (NCT02520778, NCT02079740, NCT00878449, and NCT01989585). While these trials do not necessarily aim to explore the senolytic activity of ABT-263, elimination of senescent cells with this drug may account for enhanced efficacy. With the current study, we provide proof-of-concept that BH3-mimetics may be used as senolytics for stalling cancer growth of tumors in mice that have an elevated burden of senescent cells such as that observed in poorly immunogenic tumors upon DIO.

In sum, our data suggest that the pro-tumoral effects of obesity occur, at least in part, via an elevated burden of tumoral cellular senescence. Collectively, our findings reveal that senolytic therapies, such as those based on BH3 mimetics, may be beneficial in oncology when patients have an elevated BMI and, more broadly, that body composition may be a factor to consider in selection of cancer therapy.

Material and Methods

Histological Preparation of Human CRC Metastasis in Liver Biopsies. Histological human samples were obtained from the RRCancer Biobank (CRCHUM) through a collaboration with the investigator in charge, Dr. Simon Turcotte. The use of the histological samples was approved by the CÉR-CEMTL committee (Protocol 2022-2647), and no other information than the one presented in *SI Appendix*, Table S1 was provided. Lean (BMI < 25) and obese (BMI > 35) patient samples were embedded in paraffin, cut at 5 μm, and kept at room temperature in a locked cabinet. The sample preparation went as followed. Slides were heated on a hermos-block for 5 min at 100 °C before being deparaffinized in xylenes solution. Samples were then hydrated and boiled for 10 min in a citrate buffer to optimize antigen retrieval.

Immunofluorescent Detection in Human Biopsies. Immunodetection was performed following a blocking and permeabilization step with BSA 3% and Triton-X-100 0.1% for 30 min. Antibodies were incubated in blocking solution overnight and were detected using species-appropriate fluorescent-conjugated secondary antibodies. Samples were then mounted and visualized using an epifluorescence microscope (Zeiss Axio Imager).

The number of $p16^{INK4a}$-positive cells (ab241543) were determined using the colocalization finder plugin on ImageJ. $P16^{INK4a}$ and DAPI colocalized stainings were assessed using Pearson's correlation measurements in healthy and tumoral regions independently (two representative regions per sample). All analyzed regions represented 5 × 5-tiled images using a 10× objective to cover representative areas in biopsies.

Animal Models. All animal studies complied with the ARRIVE Guidelines 2.0 (detailed ARRIVE Guidelines in the *SI Appendix*, Supplementary Material File) (79). *C57BL/6J* WT mice were purchased from the Jackson Laboratory and bred in house. All strains were bred in the institute's animal facility and kept in 12h–12h light and dark cycles with free access to water and food. Animals were assigned to the different experimental groups in a randomized fashion.

DIO Model. One month prior to tumor inoculation, all 8-wk-old animals were randomly subjected to either a high-fat diet (60% lipids) or a nutritionally matched CTRL diet (10% lipids). Both diets were purchased from Research Diet. Animals were left on diet until sacrifice (14 wk of age). Animal weights were monitored weekly throughout the duration of the experiment using a digital balance.

GTT. Mice were starved for 12 h overnight. Blood glucose was measured from the tail vein using AlphaTrak2 test strips before intraperitoneal injection of 10% D-glucose in PBS (2 mg/kg of weight) and at 15, 30, 60, 120, and 240 min after.

ITT. Mice were starved for 6 h in the morning. Blood glucose was measured from the tail vein using AlphaTrak2 test strips before intraperitoneal injection of insulin (0.75 U/kg of weight) and at 30, 60, and 120 min after.

Syngeneic Tumor Inoculation and Tumor Volumetric and Weight Monitoring. To initiate tumors, we inoculated cancer cells in 12-wk-old animals by subcutaneously injecting 4×10^5 LLC cells, 5×10^5 B16-F10 cells, or 5×10^5 MC-38 cells in 100 µL of PBS 1X. These cells are of *C57BL/6J* origin, which has the advantage of being immunologically compatible with our mice strain. The tumor growth was followed at different time points by means of caliper for volumetric measures (7, 10, 12, and 14 d after inoculation) in vivo. Tumor volume was calculated with the following formula: volume = (length × width^2)/2. Tumor weight was evaluated with an analytic scale. Mice reaching predetermined endpoints such as a tumor volume reaching 500 mm^3 or a significant tumor ulceration or weight loss (>20%) were euthanized and excluded from further analysis. At the endpoint of experiments, tissues of interest were collected and processed for further analysis.

Generation of Transgenic $LLC^{LUC\text{-}mCherry}$ and In Vivo Luciferase Activity Monitoring. Murine LLC cells were cultivated in DMEM supplemented with 10% fetal bovine serum (FBS) and 1% penicillin–streptomycin. A transgene was generated via the retroviral infection of the MSCV-LUC-IRES-mCherry plasmid (referred in this paper as $LLC^{LUC\text{-}mCherry}$) as described before (80). In brief, to generate ecotropic retroviral particles, pCL-ECO and MSCV-Luciferase-IRES-mCherry vectors were cotransfected at a 1:1 ratio. Transfections of plasmid DNA in HEK293T cells were performed using Lipofectamine 2000 according to the manufacturer's instructions. For transduction, virion supernatants and fresh LLC culture media were mixed with a 1:1 ratio and supplemented with 6 µg/mL of hexadimethrine bromide. LLC cells were seeded at a rate of 1 million cells/mL in transduction media and spun at 900 g (2250 RPM, Eppendorf Centrifuge 5810 R, Rotor A-4-81 MTP/Flex) for 90 min at 24 °C. Two days following transduction, mCherry-expressing cells were sorted by FACS (BD FACSAria II Flow Cytometer) (*SI Appendix*, Fig. S3*A*). The luciferase activity of these cells was also confirmed using an IVIS (*SI Appendix*, Fig. S3*B*). The expression of mCherry was maintained after three passages of the infected LLC cells (88, 3% positive) demonstrating the stability of its expression over time (*SI Appendix*, Fig. S3*C*). We also showed that the cell cycle status (PI) and BrdU incorporation were not affected by the transduction, ensuring that $LLC^{LUC\text{-}mCherry}$ cells had a similar proliferative rate to the uninfected LLC cells (*SI Appendix*, Fig. S3*D*).

Luciferase assays were performed following manufacturer's recommendations. In brief, 150 mg of D-luciferine potassium salt per kg of animal was intraperitoneally (IP) injected 10 min prior to the imaging using an In Vivo Imaging System (IVIS; IVIS Lumina). Animals were kept anaesthetized while imaging. The luciferase activity was analyzed according to radiance (photon/second/cm^2/steradian). Tumor growth was followed at different time points by means of luciferase assay (3, 5, 7, 10, 12, and 14 d after inoculation). This strategy allowed us to monitor the tumor growth using the luciferase activity of the LLC cells in *C57Bl/6J* mice.

Histological Analysis of SA-β-gal Activity in Tumors. SA-β-gal activity assays were carried out as previously described (81). In a PBS1X-$MgCl_2$, pH5.0 buffer overnight at 4 °C, 20-µm tissue sections were incubated. The buffer was replaced by an X-Gal staining solution (5-bromo-4-chloro-3-indolyl-beta-D-galactopyranoside) (1 mg/mL X-Gal, 1 mM $MgCl_2$, 5 mM $K_3Fe(CN)_6$, 5 mM $K_4Fe(CN)_6$) in PBS 1X, pH5.0 for 6 h at 37 °C. All tumor cross sections were assessed at the same time. The reaction was stopped with 4 washes of PBS1X and imaged immediately using an epifluorescence microscope (DIC; Zeiss Axio Imager).

Immunoblotting. Protein extraction from tumors was performed with 100 to 500 mg of frozen tissues (−80 °C). Tissue was homogenized in lysis buffer (150 mM NaCl, 1%NP40, 0, 5%DOC, 50 mM Tris pH8.9) followed by the addition of the 2X detergent buffer (150 mM NaCl, 2%NP40, 1%DOC, 0, 2% SDS, 50 mM Tris pH8.9) to the samples. Both buffers were supplemented with phosphatase (1:100) and protease (1:500) inhibitors. Protein extraction was also performed on cell-sorted cells. Using a FACSAria III Cell Sorter (BD Biosciences) device, we were able to extract $CD45.2^+CD11b^+Ly6G^-CD11c^{low}F4/80^{high}CD64^+$ cells (TAMs) and $mCherry^+$ cells (cancer cells). The extraction method consists, this time, of cell lysis in RIPA 1X buffer (150 mM NaCl, 1%NP40, 0, 5%DOC, 0, 1% SDS, 50 mM Tris pH8.9), supplemented with phosphatase and protease inhibitors, followed by a freeze and thaw cycle. The protein concentration from homogenate and cell lysates was assessed using a QuantiPro BCA Assay Kit, and the wanted amount of protein (10 to 50 µg) was analyzed for each condition by the standard SDS-PAGE technique. All primary antibodies are listed in *SI Appendix*, Table S2.

Western blots quantification was all carried the same way. We quantified western blots images using ImageJ software (Mean gray area) for each analyzed protein. First, every sample on a particular membrane was normalized to its own reference protein signal (β-actin). Second, the normalized signal was rationalized on the mean of all the normalized signals of the experimental control. Every replicate (*n*) is presented as a relative signal to the mean of the experimental control signals of the same experiment.

Quantitative PCR Analysis of Tumor Lysates. RNA extraction was performed with 100 to 500 mg of frozen tissues (−80 °C) after the TRIzol Reagent Protocol. Then, 1 µg of RNA was reverse-transcribed according to the manufacturer's instructions (Applied Biological Materials Inc.). The qPCR experiments were performed using BrightGreen 2X, 250 nM of primer mix (1:1) and 40 ng of complementary DNA per reaction (7,500 Real-Time PCR System, Applied Biosystems). Expression levels of *Actb* were used to normalize the expression of the different genes. All primers used are listed in *SI Appendix*, Table S3.

Senolysis Treatment In Vivo after Tumor Inoculation. To investigate the relevance of senescent cells in tumors and their impact on tumor growth, we treated mice with navitoclax (ABT-263), a senolytic targeting BCL-2 family members and inhibiting their antiapoptotic action (39, 74), via gavage. Following the same in vivo experimental paradigm as before, we treated DIO and CTRL mice for five consecutive days, starting on the 7th day postinoculation, with either ABT-263 (75 mg/kg) or vehicle (DMSO) resuspended in corn oil via gavage. Mice were randomly assigned to receive either the compound or the vehicle prior to tumor inoculation. As before, tumors were monitored every second day for 2 wk by means of luciferase activity and caliper measurements, and mice reaching the predetermined endpoints were euthanized and excluded from further analysis. At the endpoint of experiments, the tumors were collected and processed for FACS analysis.

Tumor Microenvironment Characterization with FACS. Tumors were collected in Dulbecco's modified Eagle's medium (DMEM) and homogenized in a solution of 500 U/mL Collagenase IV, 10 µg/mL Liberase TL, and 100 U/mL Dnase I for 30 min at 37 °C under gentle shaking every 5 min. Homogenates were then filtered with a 70-µm cell strainer and washed in PBS supplemented with 10% FBS. Samples were then subjected to 1X RBC Lysis Buffer for 5 min, and

the remaining cells were resuspended in PBS for zombie aqua viability staining for 15 min at room temperature. The cell suspensions were then incubated with LEAF-purified anti-mouse CD16/32 for 10 min at 4 °C to block Fc receptors. Cells were then incubated for 25 min at 4 °C with wanted mixes of the following antibodies (all detailed in *SI Appendix*, Table S2): Alexa Fluor® 700 anti-mouse CD45.2, Brilliant Violet 711™ anti-mouse/human CD11b, PE/CY7 anti-mouse F4/80, APC/CY7 anti-mouse Ly6G, Brilliant Violet 785™ anti-mouse CD11c, APC anti-mouse CD64, and APC anti-mouse CD31. Macrophages, neutrophils, and endothelial cells were gated as macrophages (Zombie$^-$, CD45.2$^+$, CD11b$^+$, Ly6G$^-$, CD11c$^{-/low}$ (to discriminate DCs), F4/80^{high}, and CD64$^+$), neutrophils (Zombie$^-$, CD45.2$^+$, CD11b$^+$, and Ly-6G^{high}), and endothelial cells (Zombie$^-$, CD45.2$^-$, and CD31$^+$). In addition, cancer cells (LLC cells) were detected by their endogenous mCherry expression (mCherry$^+$ cells). FACS was performed on a Fortessa X20 device with Diva software, and data were analyzed using FlowJo Software.

Single-Cell Analysis of SA-β-gal Activity in Tumors. The in vitro protocol for the detection of SA-β-gal$^+$ cells using 5-dodecanoylaminofluorescein di-β-D-galactopyranoside (C_{12}FDG) published in Nature Protocol (66) was adapted for the single-cell detection of SA-β-gal$^+$ cells in our in vivo settings. We dissected and homogenized tumors as mentioned above and used the same gating strategies as before to identify macrophages, neutrophils, endothelial cells, and cancer cells. Then, we increased the internal pH of lysosomes using bafilomycin A1 to increase the specificity of our assay for the detection of senescent cells. Following an hour incubation of 100 μM bafilomycin A1 (37 °C; 5% CO_2), 2 μM of C_{12}FDG, a β-galactosidase substrate emitting green fluorescence upon enzymatic reaction, was added to the sample for 20 min (37 °C; 5% CO_2), rendering the detection of SA-β-gal$^+$ cells possible by flow cytometry on a Fortessa X20 (BD Biosciences) device. Data were further analyzed using FlowJo software.

Cell Cycle Analysis in Tumors. We dissected and homogenized tumors as mentioned above. Then, we analyzed the cycle state of cancer cells (mCherry$^+$) using DAPI (75 μM) as previously described (G0/G1 = 2n, S = 2n~4n, and G2/M = 4n) (82). The samples were permeabilized and fixed following the manufacturer's instructions (Cytofix/Cytoperm kit). On the day of the acquisition at the Fortessa X20 device (BD Biosciences), we thawed cells and performed the DAPI staining right before the FACS acquisition.

Caspase 3/7 Activation Analysis. We dissected whole tumors and extracted proteins from tumor lysates as described above. We then evaluated the activity of Caspase3 and Caspase7 in our samples by using the Caspase-Glo® 3/7 Assay kit (Promega). In brief, we assessed the intensity of bioluminescence produced from 15 μg of protein and subsequently added the proluminescent caspase-3/7 DEVD-aminoluciferin substrate with a proprietary thermostable luciferase in a reagent optimized for caspase-3/7 activity for 2 h. We then subtracted the counts per second (CPS) of blank wells (RIPA 1X) from every sample and compared the amount of luminescence between groups at each time point.

Material and Data Availability. All materials as well as data used in this project are included in the different sections of the manuscript and referenced in the *SI Appendix*, Table S4.

Statistical Analysis. All experiments were performed at least 2 to 3 times. Data are presented as mean ± SEM. *P* values were considered significant when $P < 0.05$ (*), $P < 0.01$(**), or $P < 0.001$ (***). All outliers are determined with the ROUT method (Q = 1.0%). The number of minimum biological replicates (n) for consistent results was established based on previous experiments and existing literature references. At least 3 biological replicates were used for each biochemical experiment (ex vivo and in vitro), whereas 4 to 17 biological replicates per group were used for animal studies (in vivo). *N* are indicated in figure legends for each experiment.

Study Approval. All studies were approved by the Animal Care Committee of the Maisonneuve-Rosemont Hospital Research Center in agreement with the guidelines established by the Canadian Council on Animal Care.

Data, Materials, and Software Availability. All study data are included in the article and/or *SI Appendix*.

ACKNOWLEDGMENTS. P.S. holds the Wolfe Professorship in Translational Research and the Fonds de Recherche en Ophtalmologie de L'Université de Montreal (FROUM) endowed Chair, as well as a Canada Research Chair in Retinal Cell Biology. F.A.M. is the recipient of the Canada Research Chair in Epigenetics of Aging and Cancer. This work was supported by operating grants from the Canadian Institutes of Health Research (Foundation grant #148460), Heart and Stroke Foundation (G-21-0031875), and the Canadian Diabetes Association (DI-3-18-5444-PS). S.C.-G.: holds a scholarship from the Fonds de la Recherche du Québec en Santé (FRQS) and from the Montreal Diabetes Research Center (MDRC). M.N.: holds postdoctoral fellowships from the FRQS and the Cole Foundation. R.D.-M.: holds a scholarship from Le Fonds de Recherche en Ophtalmologie de l'Université de Montréal (FROUM). We thank Dr Simon Turcotte and Mme Louise Rousseau from the CR-CHUM for providing human samples through the RRCancer Biobank. We thank Dr Mikhail Sergeev for the support with the microscope, Dr Claire Viallard for teaching the xenograph model, Dr Christopher Rudd laboratory at CRHMR for kindly providing MC-38 and B16-F10 cancer cell lines, Vera Guber, Dr Gaëlle Mawambo, and Dr Natalija Popovic for their technical support and the animal facility assistants for managing the colony at the Hospital Maisonneuve-Rosemont Research Center.

Author affiliations: [a]Department of Biochemistry, Maisonneuve-Rosemont Hospital Research Centre, Université de Montréal, Montréal, QC H1T 2M4, Canada; [b]Department of Ophthalmology, Maisonneuve-Rosemont Hospital Research Centre, Université de Montréal, Montréal, QC H1T 2M4, Canada; [c]Department of Biomedical Sciences, Maisonneuve-Rosemont Hospital Research Centre, Université de Montréal, Montréal, QC H1T 2M4, Canada; [d]Department of Medicine, Maisonneuve-Rosemont Hospital Research Centre, Université de Montréal, Montréal, H1T 2M4, Canada; and [e]UNITY Biotechnology, South San Francisco, CA 94080

1. K. I. Avgerinos *et al.*, Obesity and cancer risk: Emerging biological mechanisms and perspectives. *Metabolism* **92**, 121–135 (2019).
2. E. E. Calle *et al.*, Overweight, obesity, and mortality from cancer in a prospectively studied cohort of U.S. adults. *N. Engl. J. Med.* **348**, 1625–1638 (2003).
3. D. R. Meldrum, M. A. Morris, J. C. Gambone, Obesity pandemic: Causes, consequences, and solutions-but do we have the will? *Fertil. Steril.* **107**, 833–839 (2017).
4. M. J. Khandekar, P. Cohen, B. M. Spiegelman, Molecular mechanisms of cancer development in obesity. *Nat. Rev. Cancer* **11**, 886–895 (2011).
5. C. H. O'Flanagan, L. W. Bowers, S. D. Hursting, A weighty problem: Metabolic perturbations and the obesity-cancer link. *Horm. Mol. Biol. Clin. Investig.* **23**, 47–57 (2015).
6. T. Deng *et al.*, Obesity, inflammation, and cancer. *Annu. Rev. Pathol.* **11**, 421–449 (2016).
7. N. M. Iyengar *et al.*, Obesity and cancer mechanisms: Tumor microenvironment and inflammation. *J. Clin. Oncol.* **34**, 4270–4276 (2016).
8. R. Kolb, F. S. Sutterwala, W. Zhang, Obesity and cancer: Inflammation bridges the two. *Curr. Opin. Pharmacol.* **29**, 77–89 (2016).
9. C. Franceschi, Healthy ageing in 2016: Obesity in geroscience–is cellular senescence the culprit? *Nat. Rev. Endocrinol.* **13**, 76–78 (2017).
10. B. K. Kennedy *et al.*, Geroscience: Linking aging to chronic disease. *Cell* **159**, 709–713 (2014).
11. J. M. van Deursen, The role of senescent cells in ageing. *Nature* **509**, 439–446 (2014).
12. A. Calcinotto *et al.*, Cellular senescence: Aging, cancer, and injury. *Physiol. Rev.* **99**, 1047–1078 (2019).
13. D. Munoz-Espin, M. Serrano, Cellular senescence: From physiology to pathology. *Nat. Rev. Mol. Cell Biol.* **15**, 482–496 (2014).
14. M. Storer *et al.*, Senescence is a developmental mechanism that contributes to embryonic growth and patterning. *Cell* **155**, 1119–1130 (2013).
15. D. Munoz-Espin *et al.*, Programmed cell senescence during mammalian embryonic development. *Cell* **155**, 1104–1118 (2013).
16. M. Demaria *et al.*, An essential role for senescent cells in optimal wound healing through secretion of PDGF-AA. *Dev. Cell* **31**, 722–733 (2014).
17. F. Binet *et al.*, Neutrophil extracellular traps target senescent vasculature for tissue remodeling in retinopathy. *Science* **369**, eaay5356 (2020).
18. S. Crespo-Garcia *et al.*, Pathological angiogenesis in retinopathy engages cellular senescence and is amenable to therapeutic elimination via BCL-xL inhibition. *Cell Metab.* **33**, 818–832.e7 (2021).
19. M. Oubaha *et al.*, Senescence-associated secretory phenotype contributes to pathological angiogenesis in retinopathy. *Sci. Transl. Med.* **8**, 362ra144 (2016).
20. T. Eggert *et al.*, Distinct functions of senescence-associated immune responses in liver tumor surveillance and tumor progression. *Cancer Cell* **30**, 533–547 (2016).
21. J. P. Coppe *et al.*, The senescence-associated secretory phenotype: The dark side of tumor suppression. *Annu. Rev. Pathol.* **5**, 99–118 (2010).
22. T. Minamino *et al.*, A crucial role for adipose tissue p53 in the regulation of insulin resistance. *Nat. Med.* **15**, 1082–1087 (2009).
23. M. J. Schafer *et al.*, Exercise prevents diet-induced cellular senescence in adipose tissue. *Diabetes* **65**, 1606–1615 (2016).
24. M. Ogrodnik *et al.*, Cellular senescence drives age-dependent hepatic steatosis. *Nat. Commun.* **8**, 15691 (2017).

25. B. Gustafson, A. Nerstedt, U. Smith, Reduced subcutaneous adipogenesis in human hypertrophic obesity is linked to senescent precursor cells. *Nat. Commun.* **10**, 2757 (2019).
26. Q. Li *et al.*, Obesity and hyperinsulinemia drive adipocytes to activate a cell cycle program and senesce. *Nat. Med.* **27**, 1941–1953 (2021).
27. A. K. Palmer *et al.*, Targeting senescent cells alleviates obesity-induced metabolic dysfunction. *Aging Cell* **18**, e12950 (2019).
28. M. J. Schafer, J. D. Miller, N. K. LeBrasseur, Cellular senescence: Implications for metabolic disease. *Mol. Cell Endocrinol.* **455**, 93–102 (2017).
29. T. Tchkonia *et al.*, Fat tissue, aging, and cellular senescence. *Aging Cell* **9**, 667–684 (2010).
30. W. Trim, J. E. Turner, D. Thompson, Parallels in immunometabolic adipose tissue dysfunction with ageing and obesity. *Front. Immunol.* **9**, 169 (2018).
31. D. V. Faget, Q. Ren, S. A. Stewart, Unmasking senescence: Context-dependent effects of SASP in cancer. *Nat. Rev. Cancer* **19**, 439–453 (2019).
32. A. R. Davalos *et al.*, Senescent cells as a source of inflammatory factors for tumor progression. *Cancer Metastasis Rev.* **29**, 273–283 (2010).
33. D. Liu, P. J. Hornsby, Senescent human fibroblasts increase the early growth of xenograft tumors via matrix metalloproteinase secretion. *Cancer Res.* **67**, 3117–3126 (2007).
34. L. W. Qian *et al.*, Radiation-induced increase in invasive potential of human pancreatic cancer cells and its blockade by a matrix metalloproteinase inhibitor, CGS27023. *Clin. Cancer Res.* **8**, 1223–1227 (2002).
35. R. P. Czekay *et al.*, PAI-1: An integrator of cell signaling and migration. *Int. J. Cell Biol.* **2011**, 562481 (2011).
36. D. E. Vaughan *et al.*, Plasminogen activator inhibitor-1 is a marker and a mediator of senescence. *Arterioscler. Thromb. Vasc. Biol.* **37**, 1446–1452 (2017).
37. P. A. Ortiz-Montero, A. Londoño-Vallejo, J. -P. Vernot, Senescence-associated IL-6 and IL-8 cytokines induce a self- and cross-reinforced senescence/inflammatory milieu strengthening tumorigenic capabilities in the MCF-7 breast cancer cell line. *Cell Commun. Signal.* **15**, 17 (2017).
38. W. Xue *et al.*, Senescence and tumour clearance is triggered by p53 restoration in murine liver carcinomas. *Nature* **445**, 656–660 (2007).
39. Y. Zhu *et al.*, Identification of a novel senolytic agent, navitoclax, targeting the Bcl-2 family of anti-apoptotic factors. *Aging Cell* **15**, 428–435 (2016).
40. Y. Zhu *et al.*, The Achilles' heel of senescent cells: From transcriptome to senolytic drugs. *Aging Cell* **14**, 644–658 (2015).
41. E. Gonzalez-Gualda *et al.*, A guide to assessing cellular senescence in vitro and in vivo. *FEBS J.* **288**, 56–80 (2021).
42. J. Chang *et al.*, Clearance of senescent cells by ABT263 rejuvenates aged hematopoietic stem cells in mice. *Nat. Med.* **22**, 78–83 (2016).
43. R. Yosef *et al.*, Directed elimination of senescent cells by inhibition of BCL-W and BCL-XL. *Nat. Commun.* **7**, 11190 (2016).
44. S. T. Diepstraten *et al.*, The manipulation of apoptosis for cancer therapy using BH3-mimetic drugs. *Nat. Rev. Cancer* **22**, 45–64 (2022).
45. M. Xu *et al.*, Senolytics improve physical function and increase lifespan in old age. *Nat. Med.* **24**, 1246–1256 (2018).
46. K. J. Mylonas *et al.*, Cellular senescence inhibits renal regeneration after injury in mice, with senolytic treatment promoting repair. *Sci. Transl. Med.* **13**, eabb0203 (2021).
47. T. J. Bussian *et al.*, Clearance of senescent glial cells prevents tau-dependent pathology and cognitive decline. *Nature* **562**, 578–582 (2018).
48. L. Gandhi *et al.*, Phase I study of Navitoclax (ABT-263), a novel Bcl-2 family inhibitor, in patients with small-cell lung cancer and other solid tumors. *J. Clin. Oncol.* **29**, 909–916 (2011).
49. A. K. Sharma *et al.*, The senolytic drug navitoclax (ABT-263) causes trabecular bone loss and impaired osteoprogenitor function in aged mice. *Front. Cell Dev. Biol.* **8**, 354 (2020).
50. A. Kaefer *et al.*, Mechanism-based pharmacokinetic/pharmacodynamic meta-analysis of navitoclax (ABT-263) induced thrombocytopenia. *Cancer Chemother. Pharmacol.* **74**, 593–602 (2014).
51. C. M. Rudin *et al.*, Phase II study of single-agent navitoclax (ABT-263) and biomarker correlates in patients with relapsed small cell lung cancer. *Clin. Cancer Res.* **18**, 3163–3169 (2012).
52. V. J. Carpenter, T. Saleh, D. A. Gewirtz, Senolytics for cancer therapy: Is all that glitters really gold? *Cancers (Basel)* **13**, 723 (2021).
53. B. Z. Xue Hao *et al.*, Sensitization of ovarian tumor to immune checkpoint blockade by boosting senescence- associated secretory phenotype. *iScience* **24**, 102016 (2021).
54. M. Demaria *et al.*, Cellular senescence promotes adverse effects of chemotherapy and cancer relapse. *Cancer Discov.* **7**, 165–176 (2017).
55. P. G. Prasanna *et al.*, Therapy-induced senescence: Opportunities to improve anticancer therapy. *J. Natl. Cancer Inst.* **113**, 1285–1298 (2021).
56. B. Wang, J. Kohli, M. Demaria, Senescent cells in cancer therapy: Friends or foes? *Trends Cancer* **6**, 838–857 (2020).
57. A. Toso *et al.*, Enhancing chemotherapy efficacy in Pten-deficient prostate tumors by activating the senescence-associated antitumor immunity. *Cell Rep.* **9**, 75–89 (2014).
58. F. Jochems *et al.*, The cancer SENESCopedia: A delineation of cancer cell senescence. *Cell Rep.* **36**, 109441 (2021).
59. M. J. Yousefzadeh *et al.*, An aged immune system drives senescence and ageing of solid organs. *Nature* **594**, 100–105 (2021).
60. A. E. Ringel *et al.*, Obesity shapes metabolism in the tumor microenvironment to suppress anti-tumor immunity. *Cell* **183**, 1848–1866.e26 (2020).
61. L. Prata *et al.*, Senescent cell clearance by the immune system: Emerging therapeutic opportunities. *Semin. Immunol.* **40**, 101275 (2018).
62. J. S. Bertram, P. Janik, Establishment of a cloned line of Lewis Lung Carcinoma cells adapted to cell culture. *Cancer Lett.* **11**, 63–73 (1980).
63. M. G. Lechner *et al.*, Immunogenicity of murine solid tumor models as a defining feature of in vivo behavior and response to immunotherapy. *J. Immunother.* **36**, 477–489 (2013).
64. S. I. Mosely *et al.*, Rational selection of syngeneic preclinical tumor models for immunotherapeutic drug discovery. *Cancer Immunol. Res.* **5**, 29–41 (2017).
65. S. Cang *et al.*, ABT-199 (venetoclax) and BCL-2 inhibitors in clinical development. *J. Hematol. Oncol.* **8**, 129 (2015).
66. F. Debacq-Chainiaux *et al.*, Protocols to detect senescence-associated beta-galactosidase (SA-betagal) activity, a biomarker of senescent cells in culture and in vivo. *Nat. Protoc.* **4**, 1798–1806 (2009).
67. B. Lauby-Secretan *et al.*, Body fatness and cancer-viewpoint of the IARC working group. *N. Engl. J. Med.* **375**, 794–798 (2016).
68. C. Romagosa *et al.*, p16(Ink4a) overexpression in cancer: A tumor suppressor gene associated with senescence and high-grade tumors. *Oncogene* **30**, 2087–2097 (2011).
69. A. K. Witkiewicz *et al.*, The meaning of p16(ink4a) expression in tumors: Functional significance, clinical associations and future developments. *Cell Cycle* **10**, 2497–2503 (2011).
70. L. Yu *et al.*, Complete loss of miR-200 family induces EMT associated cellular senescence in gastric cancer. *Oncogene* **41**, 26–36 (2021).
71. A. Sierra-Ramirez *et al.*, Transient metabolic improvement in obese mice treated with navitoclax or dasatinib/quercetin. *Aging (Albany NY)* **12**, 11337–11348 (2020).
72. W. H. Wilson *et al.*, Navitoclax, a targeted high-affinity inhibitor of BCL-2, in lymphoid malignancies: A phase 1 dose-escalation study of safety, pharmacokinetics, pharmacodynamics, and antitumour activity. *Lancet Oncol.* **11**, 1149–1159 (2010).
73. A. W. Roberts *et al.*, Substantial susceptibility of chronic lymphocytic leukemia to BCL2 inhibition: Results of a phase I study of navitoclax in patients with relapsed or refractory disease. *J. Clin. Oncol.* **30**, 488–496 (2012).
74. T. J. Kipps *et al.*, A phase 2 study of the BH3 mimetic BCL2 inhibitor navitoclax (ABT-263) with or without rituximab, in previously untreated B-cell chronic lymphocytic leukemia. *Leuk. Lymphoma* **56**, 2826–2833 (2015).
75. M. S. Cragg *et al.*, Treatment of B-RAF mutant human tumor cells with a MEK inhibitor requires Bim and is enhanced by a BH3 mimetic. *J. Clin. Invest.* **118**, 3651–3659 (2008).
76. M. S. Cragg *et al.*, Gefitinib-induced killing of NSCLC cell lines expressing mutant EGFR requires BIM and can be enhanced by BH3 mimetics. *PLoS Med.* **4**, 1681–1689; discussion 1690 (2007).
77. Y. Gong *et al.*, Induction of BIM is essential for apoptosis triggered by EGFR kinase inhibitors in mutant EGFR-dependent lung adenocarcinomas. *PLoS Med.* **4**, e294 (2007).
78. A. Lopez *et al.*, Co-targeting of BAX and BCL-XL proteins broadly overcomes resistance to apoptosis in cancer. *Nat. Commun.* **13**, 1199 (2022).
79. N. Percie du Sert *et al.*, Reporting animal research: Explanation and elaboration for the ARRIVE guidelines 2.0. *PLoS Biol.* **18**, e3000411 (2020).
80. M. Neault, F. A. Mallette, S. Richard, miR-137 modulates a tumor suppressor network-inducing senescence in pancreatic cancer cells. *Cell Rep.* **14**, 1966–1978 (2016).
81. G. P. Dimri *et al.*, A biomarker that identifies senescent human cells in culture and in aging skin in vivo. *Proc. Natl. Acad. Sci. U.S.A.* **92**, 9363–9367 (1995).
82. P. Pozarowski, Z. Darzynkiewicz, Analysis of cell cycle by flow cytometry. *Methods Mol Biol* **281**, 301–311 (2004).
83. M. Ogrodnik *et al.*, Obesity-induced cellular senescence drives anxiety and impairs neurogenesis. *Cell Metab.* **29**, 1233 (2019).
84. K. Chatsirisupachai *et al.*, A human tissue-specific transcriptomic analysis reveals a complex relationship between aging, cancer, and cellular senescence. *Aging Cell* **18**, e13041 (2019).